ACS Partner Journal

CHEMICAL & BIOMEDICAL IMAGING

Open Access

pubs.acs.org/ChemBioImaging

Article

Fluorescence Imaging Using Deep-Red Indocyanine Blue, a Complementary Partner for Near-Infrared Indocyanine Green

Rananjaya S. Gamage and Bradley D. Smith*

Cite This: *Chem. Biomed. Imaging* 2024, 2, 384−397

Read Online

ACCESS | Metrics & More | Article Recommendations | Supporting Information

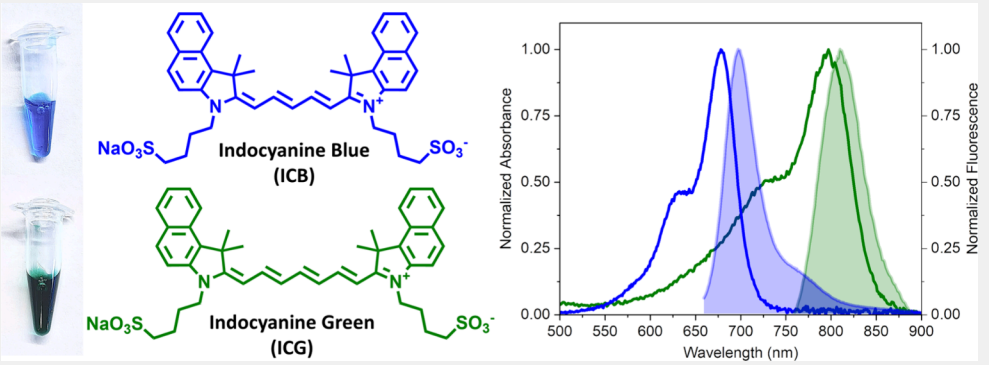

ABSTRACT: Indocyanine Blue (ICB) is the deep-red pentamethine analogue of the widely used clinical near-infrared heptamethine cyanine dye Indocyanine Green (ICG). The two fluorophores have the same number of functional groups and molecular charge and vary only by a single vinylene unit in the polymethine chain, which produces a predictable difference in spectral and physicochemical properties. We find that the two dyes can be employed as a complementary pair in diverse types of fundamental and applied fluorescence imaging experiments. A fundamental fluorescence spectroscopy study used ICB and ICG to test a recently proposed Förster Resonance Energy Transfer (FRET) mechanism for enhanced fluorescence brightness in heavy water (D_2O). The results support two important corollaries of the proposal: (a) the strategy of using heavy water to increase the brightness of fluorescent dyes for microscopy or imaging is most effective when the dye emission band is above 650 nm, and (b) the magnitude of the heavy water florescence enhancement effect for near-infrared ICG is substantially diminished when the ICG surface is dehydrated due to binding by albumin protein. Two applied fluorescence imaging studies demonstrated how deep-red ICB can be combined with a near-infrared fluorophore for paired agent imaging in the same living subject. One study used dual-channel mouse imaging to visualize increased blood flow in a model of inflamed tissue, and a second mouse tumor imaging study simultaneously visualized the vasculature and cancerous tissue in separate fluorescence channels. The results suggest that ICB and ICG can be incorporated within multicolor fluorescence imaging methods for perfusion imaging and hemodynamic characterization of a wide range of diseases.

KEYWORDS: *fluorescence imaging, perfusion imaging, tumor imaging, heavy water, mouse imaging, cell microscopy*

INTRODUCTION

Indocyanine Green (ICG) is a heptamethine cyanine dye (Scheme 1) with near-infrared absorption and fluorescence emission wavelengths. For more than 60 years, ICG has been used clinically for various types of diagnostic and imaging procedures.[1] This includes diagnostic methods that assess liver function, cardiac output, or blood volume and imaging methods for visualizing choroidal blood flow, revascularized tissue, or exposed tumors during surgery.[2−6] Although ICG is a water-soluble dye, its amphiphilic molecular structure promotes dye self-aggregation at concentrations >5 μM or reversible association with hydrophobic sites on proteins or membranes.[7] Upon intravenous dosing, ICG rapidly binds to blood proteins, especially albumin, and within a few minutes, it is cleared through the liver as an unchanged molecule and excreted into the intestines as a component of the bile juice. The rapid clearance is a major reason that the clinical safety record of ICG is quite favorable. The long-wavelength near-infrared light used for ICG fluorescence excitation and detection can penetrate relatively deeply through the skin and tissue because there is negligible absorption by endogenous pigments and reduced scattering of the light.

Received: January 24, 2024
Revised: April 18, 2024
Accepted: April 28, 2024
Published: May 2, 2024

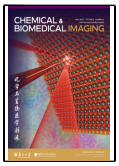

https://doi.org/10.1021/cbmi.4c00008
Chem. Biomed. Imaging 2024, 2, 384−397

Scheme 1. Chemical Structures of ICB and ICG

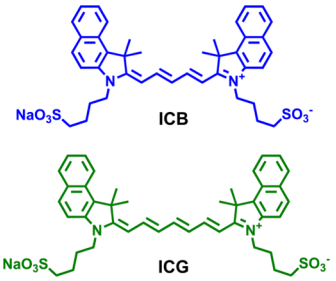

However, ICG is known for several clinical performance limitations including chemical instability in aqueous solution,[8] which restricts its clinical use to 6 h after dose reconstitution, and moderate susceptibility to photobleaching.[9] In addition, ICG self-aggregation or albumin association means the spectral properties, including fluorescence quantum yield and electronic excited state lifetime, are concentration dependent.[10] Efforts to mitigate these drawbacks have included strategies that encapsulate ICG within protective nanocapsules such as liposomes, proteins, or hyperbranched polymers.[11] There are also preclinical and clinical protocols that combine ICG with other fluorescent dyes with different wavelengths for multicolor imaging and sensing applications.[12−14] The feasibility of this approach is enhanced by ongoing advances in camera technology that enables advanced methods of multicolor and lifetime imaging.[15,16]

As part of an ongoing project to develop structural analogues of ICG with customized imaging properties,[9,17] we decided to evaluate the pentamethine version of ICG which we call Indocyanine Blue (ICB; see Scheme 1). The chemical synthesis of ICB has been reported,[18] but it also can be purchased from several different commercial vendors at an affordable price and in a relatively large amount. Despite its ready availability, there are very few published studies of ICB chemical and spectral properties[18,19] and only one report noting its propensity to self-aggregate at high concentration in aqueous solution.[20] In terms of biomedical imaging, a short communication in 1979 suggested a potential use of ICB for choroidal angiography, but the idea has not been pursued further in any subsequent publication.[21] Here, we describe a detailed comparison of ICG and ICB and present our results as three sets of distinct findings. First, we measure and compare the physicochemical and spectral properties of these two homologous dyes, which differ by a single vinylene unit in the polymethine chain. Second, we employ the two fluorophores as a complementary pair in a fluorescence spectroscopy study that supports a recently proposed photophysical explanation for enhanced dye fluorescence brightness in heavy water, and we test two important corollaries of the proposed mechanism. Third, we demonstrate the high potential of these dyes as a complementary pair of fluorescence imaging agents in a related collection of dual-channel, cell microscopy, and mouse tumor imaging studies.

RESULTS AND DISCUSSION

Comparison of Chemical and Photophysical Properties

Summarized in Table 1 are the key photophysical properties of ICB and ICG in water. Consistent with the difference of a single vinylene unit in the polymethine chain, the absorption/emission maxima wavelengths for heptamethine ICG are 100 nm longer than the maxima peaks for ICB and the molar absorption coefficient (ϵ) is larger.[22] The fluorescence quantum yield for an aqueous solution of ICB (ϕ_F = 5.0%) is higher than that of ICG (ϕ_F = 2.9%) which matches the relative difference in electronic excited state lifetimes obtained using time-correlated single photon counting (see Figure S3). Defining brightness as $\epsilon \times \phi_F$, we find that a low concentration solution of ICG is 30% brighter than an equivalent concentration of ICB.

Dye amphiphilicity was assessed using three separate experimental criteria. The first was association with albumin protein which is well-known to have a hydrophobic pocket that accepts amphiphilic dyes.[24] An albumin tryptophan quenching assay was employed to measure dissociation constants (K_d) for dye binding to bovine serum albumin (BSA) in water (Figure S4).[17,24] There was similarly high affinity with measured K_d values of (1.77 ± 0.19) μM for ICG and (2.40 ± 0.32 μM) for ICB. The second comparison of amphiphilicity determined the propensity to form dye self-aggregates in water. As shown by the absorption spectra in Figure 1a, low micromolar solutions of ICG exhibited two major peaks, one corresponding to the free monomer dye in solution and a blue-shifted band corresponding to a dye H-aggregate.[25] In both cases, the fraction of H-aggregate increased with higher dye concentration, and at any one dye concentration, the ICG sample exhibited a higher fraction of H-aggregate than the ICB sample as judged by the ratio of peaks. Addition of BSA to these dye samples produced two effects on the absorption spectra that indicate binding of monomeric dye by the BSA:[26−28] the fraction of H-aggregate peak decreased, and the absorption band for the monomeric form of each dye was red-shifted along with an increase in fluorescence brightness (Figure 1b). The third comparison of amphiphilicity measured Log P for dye partitioning between a layer of 1-octanol and an aqueous layer composed of HEPES buffer (50 mM HEPES, 100 mM NaCl, pH 7.4).[26] Notably, there was >1000-fold difference in the partitioning ratio as illustrated vividly by the photographs in Figure S2. That is, ICG preferred the 1-octanol layer with a measured Log P value of 2.05, whereas ICB preferred the aqueous layer with a measured Log P value of −1.16. Partitioning of each dye into the aqueous layer increased if it included BSA to bind the dye (Figure S2). Together, the three sets of experiments reveal quantitative differences in amphiphilic behavior; ICB is much more hydrophilic than

Table 1. Photophysical Properties of ICB and ICG in Water at Room Temperature

dye	λ_{max}^{abs} (nm)	λ_{max}^{em} (nm)	ϵ^a ($M^{-1}cm^{-1}$)	R^2	ϕ_F [%][b]	τ^c (ns)	brightness[d]	Log P^e	albumin dissociation constant (μM)
ICB	680	705	167 000	0.998	5.0 ± 0.1[f]	0.56	28 000	−1.16 ± 0.5	2.40 ± 0.32
ICG	780	805	224 000	0.999	2.9 ± 0.2[g]	0.31	37 000	2.05 ± 0.3	1.77 ± 0.19

[a]Molar absorption coefficient. [b]Fluorescence quantum yield. [c]Fluorescence lifetime. [d]Brightness = $\epsilon \times \phi_F$. [e]1-Octanol partition coefficient; aqueous layer is HEPES buffer, pH 7.4. [f]ϕ_F for ICB was measured relative to Methylene Blue in water (2.0%).[23] [g]Ref 8.

https://doi.org/10.1021/cbmi.4c00008
Chem. Biomed. Imaging 2024, 2, 384−397

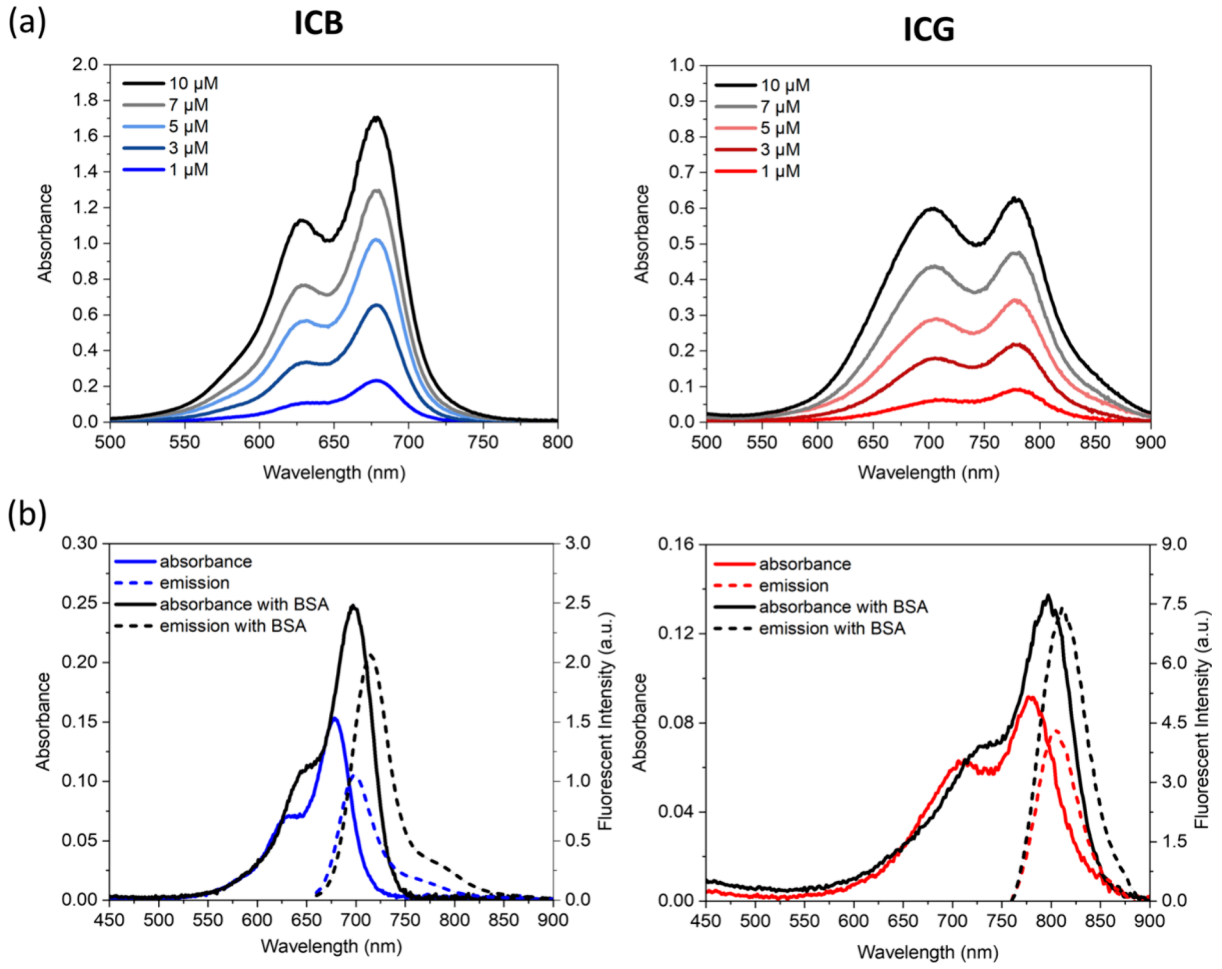

Figure 1. (a) Concentration-dependent aggregation of ICB and ICG in PBS pH 7.4. (b) Absorbance and emission (ex: 610 nm for ICB, 710 nm for ICG; slit width: 3 nm) spectra of ICB and ICG in PBS pH 7.4 and spectral shifts upon BSA addition. In all cases, the dye concentration is 1 μM.

ICG and less likely to self-aggregate in aqueous solution, but it has a similar high affinity for albumin protein.

Chemical stability of the two dyes was assessed under two different environmental conditions. The first set of stability experiments examined a solution of dye at 1 mM in pure water with very little exposure to light, a condition that mimics the typical ICG solution that is prepared in the clinic. Previously, we used an NMR spectroscopy analysis method to show that a 1 mM solution of ICG was quite degraded after storage for 6 days.[9] Repeating this chemical stability measurement with an equivalent sample of ICB (1 mM in pure water) revealed much greater chemical stability with no measurable degradation after 30 days (Figure S5a). A second set of stability experiments monitored the dye over a 2 h period in mouse serum or human serum. An in vivo imaging station was used to quantify loss of dye fluorescence for samples maintained in a multiwell plate (Figure S6). The changes in fluorescence mean pixel intensity indicated negligible loss of ICB fluorescence at all concentrations evaluated, whereas there was a significant reduction in ICG fluorescence when the dye concentration exceeded 25 μM. Photochemical stability of the two dyes was assessed by conducting standard photobleaching experiments. Separate solutions of each dye (1 μM) in PBS buffer at pH 7.4 were exposed to air and irradiated for 40 min using a 150 W xenon lamp equipped with a 620 nm long pass filter. The absorption decay curves in Figure 2 indicate a substantially slower

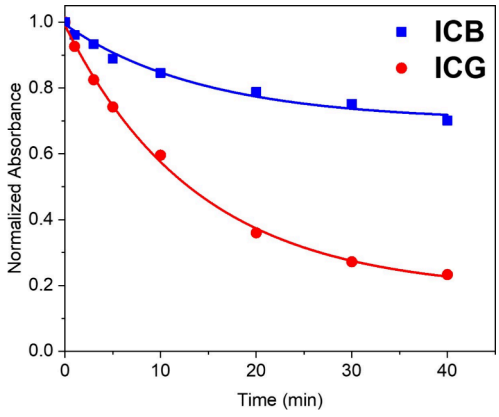

Figure 2. Photostability of ICB and ICG in separate solutions (each 1 μM in PBS buffer at pH 7.4) that were irradiated by using a 150 W xenon lamp equipped with a 620 nm long pass filter.

photobleaching rate for ICB compared to ICG. Together, these results show that ICB is substantially more stable than ICG, which matches the known increased stability of pentamethine cyanine dyes compared to heptamethine cyanine dyes.[29] A photothermal heating experiment, using a laser to illuminate ICB in water, showed good stability over repeated heating and cooling cycles (Figure 5b), suggesting high potential for applications based on photothermal heating, but

https://doi.org/10.1021/cbmi.4c00008
Chem. Biomed. Imaging 2024, 2, 384−397

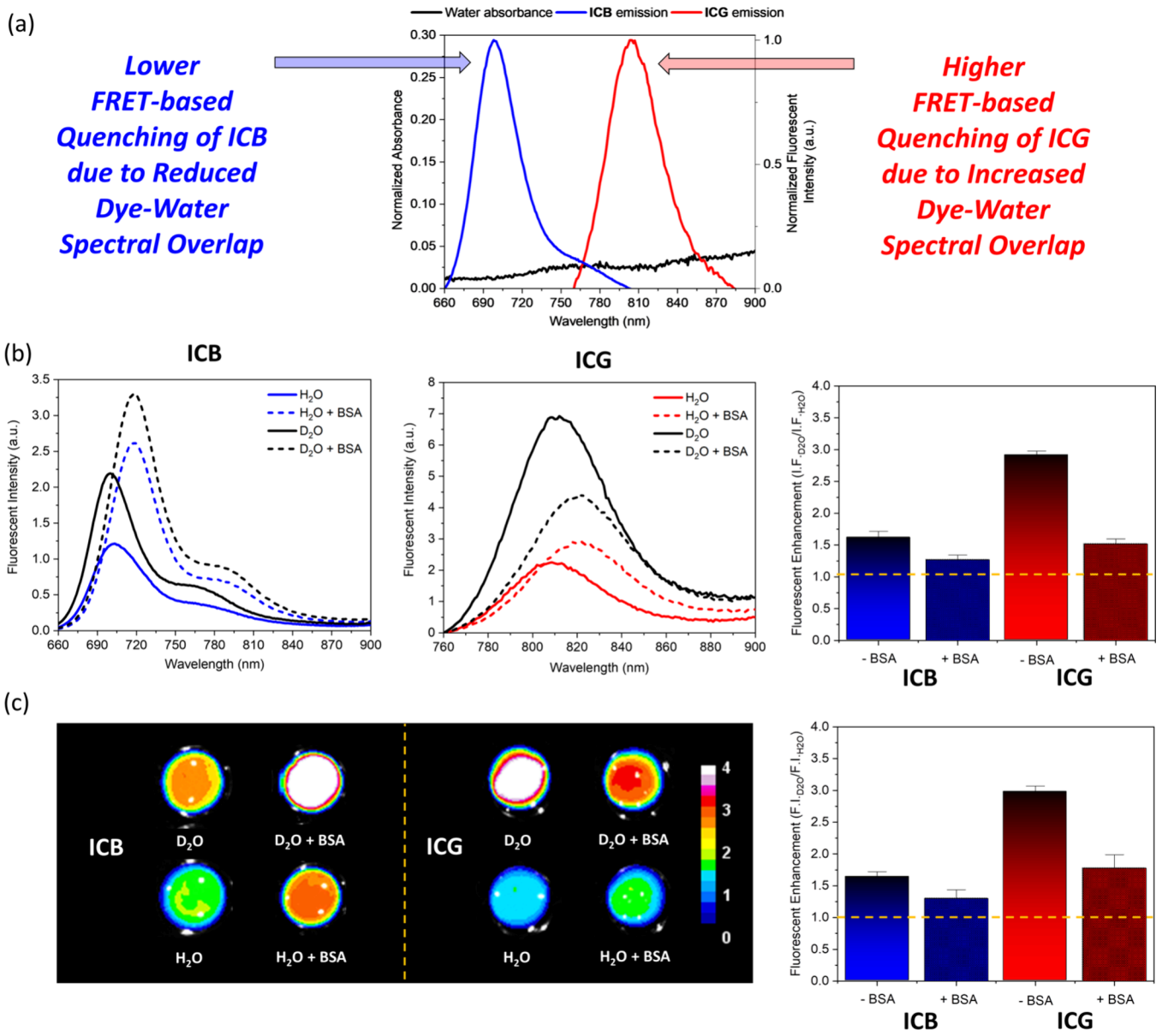

Figure 3. (a) Spectral overlap of the water absorbance and the normalized emission of ICB and ICG. (b) Fluorescence spectra for solutions of ICB or ICG in D_2O or H_2O and the effect of added BSA. I.F. is the Integrated Fluorescence for the dye emission peak. (c) Mean Pixel Intensity maps for wells containing solutions of ICB or ICG in D_2O or H_2O and the effect of added BSA. F.I. is Fluorescent Intensity and equals the mean pixel intensity for the well as a region of interest. Image acquisition settings: 700 nm filter; ex: 640/20 nm; em: 710/20 nm; exposure: 3 s; percent power: 50%; F-stop: 2; FOV: 20; binning: low; 800 nm filter; ex: 745/20 nm; em: 810/20 nm; exposure: 3 s; percent power: 50%; F-stop: 2; FOV: 20; binning: low. Dye concentration is 1 μM, and BSA concentration is 500 μM. The bar graphs show average fluorescence enhancement relative to the value in H_2O with error bars representing ± SE.

there was no sample heating using the lower power light associated with in vivo imaging.

Fluorescence Brightness in Heavy Water

It has been known for several decades that the brightness of some organic fluorophores can be increased by simply changing the solvent from light water (H_2O) to heavy water (D_2O).[30] Brightness enhancement factors of two or more have been reported, and the effect has been exploited in practical fluorescence applications,[31] especially as a potentially general method to increase image brightness and resolution in cell microscopy.[32,33] Many different photophysical processes have been proposed over the years to explain why fluorophore quenching in H_2O is usually quite efficient[34] and why it is often decreased in D_2O.[31] Recently, Maillard and co-workers suggested that a universal mechanism for fluorescence quenching in water is Förster Resonance Energy Transfer (FRET) from the electronically excited fluorophore to high energy overtones and combination transitions of O−H vibrations in the region of 700−900 nm.[35] In this scenario, an experimental switch from H_2O to D_2O eliminates these high energy O−H vibrational transitions and thus removes the associated FRET quenching pathway.[36]

It has been hypothesized that FRET quenching by water is the primary reason for the heavy water florescence enhancement effect for long wavelength cyanine dyes.[31,35] This hypothesis prompted us to study ICG and ICB as a complementary pair of cyanine dyes. Since ICG and ICB

https://doi.org/10.1021/cbmi.4c00008
Chem. Biomed. Imaging 2024, 2, 384−397

have the same number and types of functional groups, we reasoned that the switch from H_2O to D_2O should not alter the fluorescence quenching mechanism for only one of the dyes. Moreover, if FRET-based quenching is a major pathway as proposed by Maillard and co-workers,[35] then the 100 nm longer absorption/emission wavelengths of ICG should produce two specific corollaries. The first corollary is a wavelength-dependent difference in the heavy water fluorescence enhancement effect. That is, ICG should exhibit a larger heavy water florescence enhancement effect because there is increased spectral overlap of its 805 nm fluorescence emission band with the 700−900 nm H_2O absorption band, a trend that is evident in the data sets produced by previous studies.[37] In Figure 3 is a collection of fluorescence spectra and imaging data for equimolar solutions of ICG and ICB in H_2O and D_2O. In Figure 3a are the normalized emission spectra for ICB and ICG and the absorption spectrum of water. There is more spectral overlap of water with ICG than with ICB as judged by the area-under-the-curve ratios of 0.27 for H_2O/ICG and 0.18 for H_2O/ICB. The fluorescence emission spectra in Figure 3b confirm the prediction that the larger spectral overlap with ICG leads to a greater D_2O enhancement effect. That is, the ratio of integrated fluorescence intensities ($I.F._{D2O}/I.F._{H2O}$) for ICG (2.94) is substantially larger than the corresponding ratio for ICB (1.63). This trend was also apparent in fluorescence imaging experiments that used an in vivo imaging station to image microwell plates containing different solutions of ICB and ICG (Figure 3c). That is, the ratio of mean pixel intensity (MPI) values for the different images (MPI_{D2O}/MPI_{H2O}) was 2.94 for ICG and 1.56 for ICB. Finally, we confirmed that the dye excited state lifetime was relatively longer in D_2O than in H_2O as expected for a FRET-based quenching mechanism (Figure S3).

A second corollary of the FRET-based rationalization for the heavy water florescence enhancement effect is a diminished effect if the fluorophore is engaged in a protein binding process that removes water molecules from the fluorophore surface.[36] Although the FRET-based quenching process is inherently inefficient due to the small spectral overlap of the excited fluorophore with the high energy of the O−H vibrational transitions, there is considerable additivity due to the high number of independent energy-accepting water molecules that are close to the dye surface. Recently reported molecular dynamics simulations suggest that a free heptamethine cyanine dye molecule in pure aqueous solution is surrounded by a surface solvation shell composed of 100 to 200 water molecules.[36,38] Moreover, binding of the dye by albumin protein reduces the average number of water molecules surrounding the dye by about a factor of 2 (Scheme 2).[38] Since FRET efficiency has a $1/r^6$ dependence on the distance r between the excited state fluorophore as the energy donor and nearby water molecule as the energy acceptor, the number of surface water molecules should determine the amount of fluorescence quenching. This corollary was tested by acquiring ICG spectra in the presence and absence of BSA. A 1:500 ratio of dye (1 μM) to BSA (500 μM) was used to ensure that all the dye was bound by the BSA as a monomeric species (i.e., no dye aggregation in the BSA pocket). The spectral data in Figure 3b and the imaging data in Figure 3c show the same trend: the presence of BSA greatly diminished the capacity of D_2O to increase ICG florescence. Specifically, the ratio of integrated fluorescence intensities ($I.F._{D2O}/I.F._{H2O}$) for ICG was lowered from 2.94 when it was a free dye in solution to a ratio of 1.40 when ICG was bound to BSA. In the case of ICB, the presence of BSA has little impact on the heavy water florescence enhancement effect (i.e., the ratio of integrated fluorescence intensities ($I.F._{D2O}/I.F._{H2O}$) decreased from 1.56 for free ICB to 1.28 when ICB was bound to BSA). The fact that dye dehydration upon binding to BSA greatly diminishes the heavy water florescence enhancement effect for near-infrared ICG but has only a minor effect on the heavy water florescence enhancement effect for deep-red ICB is consistent with the proposed FRET-based quenching mechanism.[36]

Scheme 2. Illustration of the Surface Water Molecules Surrounding a Free Dye in Bulk Solution (Left) and a Partially Dehydrated Dye Surface When Complexed by Albumin Protein (Right)[a]

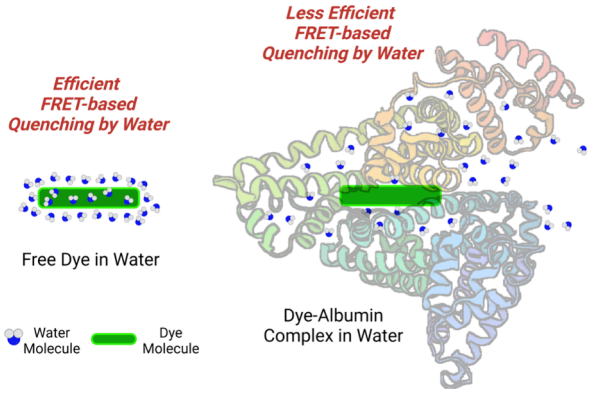

[a]The extent of dye surface dehydration is exaggerated to emphasize the point.

It is worth emphasizing that nonradiative relaxation of excited state cyanine dyes, like ICG, can potentially occur by other pathways that are activated by protein binding. In this regard, fluorescence spectroscopy studies of long-wavelength dye-binding processes in D_2O can be illuminating since they eliminate the dominating effect caused by a change in H_2O quenching. For example, it is notable that the ICB fluorescence in D_2O is enhanced by 15% upon binding to BSA, but the ICG fluorescence in D_2O is decreased by 30% (Figure 3b). This trend was confirmed by independent microwell imaging experiments that compared image intensities for solutions of dye alone with dye + BSA in various ratios of H_2O to D_2O (Figures 3c and S7). The fact that BSA quenches ICG fluorescence in D_2O is extraordinary because enhancement of cyanine dye fluorescence upon binding to albumin in H_2O is a universal phenomenon.[24,27] Since ICG self-aggregation in the BSA binding pocket is very unlikely under the experimental conditions, there must be a photophysical process that quenches the electronically excited BSA/ICG complex more efficiently than the excited state of free ICG in D_2O. A logical explanation is enhanced intersystem crossing of excited singlet state BSA/ICG to the excited triplet state (the triplet state quantum yield of ICG is in the range of 10−20% depending on microenvironment).[39,40] However, other quenching processes such as photoisomerization or reversible nucleophilic addition by a BSA cysteine cannot be currently ruled out.[41,42]

To summarize this study of heavy water effects on fluorescence, the photophysical comparison of ICB and ICG in H_2O and D_2O has demonstrated three practically important features of the heavy water fluorescence enhancement effect. (a) The strategy of using D_2O to increase the brightness of fluorescent cyanine dyes for microscopy or imaging is most

https://doi.org/10.1021/cbmi.4c00008
Chem. Biomed. Imaging 2024, 2, 384−397

effective when the dye emits at a wavelength above 650 nm.[37] (b) The large heavy water florescence enhancement effect for an amphiphilic near-infrared cyanine dye, like ICG, will be substantially diminished if the dye's surface is dehydrated due to binding with a biological site such as a protein or a membrane. (c) Fluorescence spectroscopy studies of supramolecular processes that bind a long-wavelength fluorescent dye should consider studies in D_2O as an experimental tactic that eliminates the masking effect caused by the extensive fluorescence quenching by H_2O and may reveal more subtle dye excited state relaxation pathways.

Fluorescence Bioimaging

As a prelude to in vivo fluorescence imaging studies, a series of informative cell culture experiments were conducted. First, a set of standard MTT assays, using three different cancer cell lines (HT-29 human colorectal adenocarcinoma,[43] A549 human lung adenocarcinoma,[44] and U87 human glioblastoma[45]) found that added ICB, like ICG, had no deleterious effect on cell metabolic activity (Figure S8). Next, a subsequent series of fluorescence microscopy experiments examined HT-29 cells treated with ICB. Previous work by Onda and co-workers concluded that ICG permeates HT-29 cells by two independent pathways: (a) direct association with the cell plasma membrane followed by clathrin-dependent endocytosis and (b) facilitated transport through the plasma membrane by endogenous organic anion transporter proteins.[43] We find that analogous cell experiments using ICB have produced the same results. That is, cell microscopy experiments that incubated HT-29 cells with 5 μM ICB for 2 h observed fluorescent puncta inside the cells with significantly less cell uptake at 4 °C compared to 37 °C (Figures 4A and S9). Both observations are diagnostic of cell entry by endocytosis. Additional cell microscopy studies determined that ICB uptake by the cells was diminished when the cells were pretreated with sulfobromophthalein (BSP), a known inhibitor of organic anion transporters (Figures 4B and S10). Further microscopy experiments coincubated cells with ICB and two different fluorescent organelle markers, namely, Mitotracker or Lysotracker, and determined the amount of fluorescence colocalization. After a 2 h incubation, most of the ICB fluorescence was observed in the mitochondria, but after incubation for 24 h, the ICB fluorescence was primarily in the lysosomes (Figures 4c and S11). This time-dependent pattern of organelle localization is very similar to that reported for ICG.[43] Thus, we conclude that ICB and ICG interacted with the cells in a similar manner. That is, they entered the cells by endocytosis or by facilitated transport through endogenous organic anion transporters, and they initially accumulated in mitochondria; however, over time, they translocated to cell lysosomes.

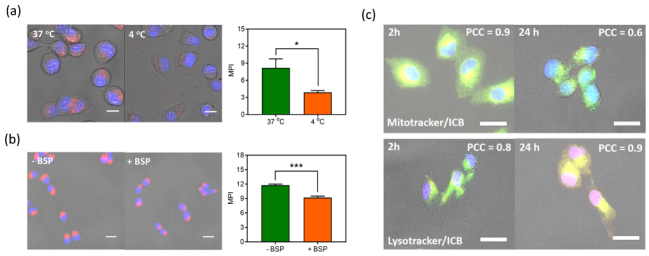

Figure 4. (a) Qualitative and quantitative analysis of live cell imaging of HT-29 cells incubated with 5 μM ICB (red) for 2 h at either 37 or 4 °C followed by a 10 min incubation with 3 μM Hoechst 33332 (blue). Length scale bar = 10 μm. (b) Qualitative and quantitative analysis of fixed cell imaging of HT-29 cells incubated with 5 μM ICB (red) for 2 h in the presence or absence of membrane transport inhibitor sulfobromopthalein (BSP). Length scale bar = 10 μm. (c) Images of HT-29 cells that were incubated with ICB for 2 or 24 h, then treated with Mitotracker or Lysotracker for 15 min, fixed with paraformaldehyde, and then stained with 3 μM Hoechst 33332 (blue). The colocalization of ICB with the tracker dye is indicated as yellow. Length scale bar = 10 μm. Error bars represent ± SE. *: $p < 0.05$; ***: $p < 0.001$. MPI is Mean Pixel Intensity; PCC is Pearson Correlation Coefficient.

For mouse imaging, we used a commercial in vivo imaging station that was equipped with multiple LEDs as the light sources and a back illuminated CCD for image detection. As noted by others,[46] this camera design detects deep-red light with high sensitivity and we have used it often for imaging the location of deep-red fluorescent probes in living mice.[47,48] Deep-red light does not penetrate through skin and tissue as far as near-infrared light; nonetheless, we could easily image a phantom containing ICB when it was covered by several millimeters of 1% intralipid solution as a mimic of scattering biological tissue (Figure S12a). This result provided reassurance that ICB and ICG would be an effective pair of in vivo imaging agents for relatively shallow locations in a living subject.

A major reason for the long-term and ongoing clinical success of ICG is its capacity to be excreted rapidly from a living subject without structural modification. More specifically, ICG is taken into liver hepatocytes by influx transporters such as the organic anion-transporting polypeptide 1B3 (OATP1B3) and subsequently excreted to bile canaliculi by efflux transporters such as multidrug resistance *p*-glycoprotein-3 (MDR3).[49,50] With this pharmacokinetic behavior in mind, we compared the biodistribution of ICB and ICG in a living mouse after intravenous dosage. Separate cohorts of healthy female Foxn1 mice (each $N = 2$) were injected with a 10 nmol dose of either ICB or ICG. After 2 h, the mice were euthanized, and their exposed abdomen cavities were imaged. The representative fluorescence images in Figures 5a and S12b reveal a higher amount of ICG in the mouse intestines compared to ICB. Fluorescence images of the excised organs are shown in Figure 5b along with a biodistribution bar graph (Figures 5c, S12, and S13). There was significant ICG accumulation in the liver and some accumulation in the kidneys. In contrast, there was only ICB accumulation in the intestines, with negligible ICB signal in any other excised organ, including the liver. We attribute the desirable pharmacokinetic features of ICB to a favorable combination of (a) high ICB affinity for blood proteins which inhibits passive ICB extravasation from the bloodstream[51] and (b) rapid uptake into hepatocytes, presumably by OATP1B, with negligible retention within these liver cells due in part to ICB hydrophilicity (negative Log *P* value) which diminishes hydrophobic interaction with the efflux transporters and cell membranes.[49,50]

These mouse biodistribution results suggested to us that ICB would likely be an effective deep-red fluorescent marker for imaging blood perfusion. We tested this possibility by conducting mouse imaging experiments that monitored changes in blood perfusion induced by inflammation. In recent years, fluorescence imaging has emerged as a valuable tool for diagnosing inflammatory diseases and conditions.[52−55]

https://doi.org/10.1021/cbmi.4c00008
Chem. Biomed. Imaging 2024, 2, 384−397

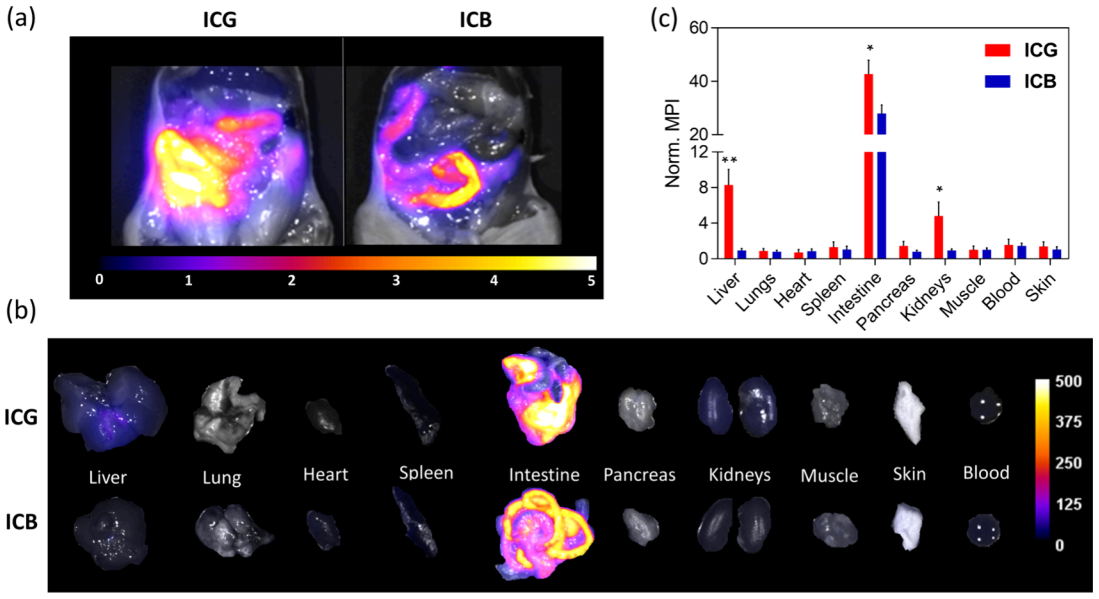

Figure 5. (a) Overlaid brightfield and fluorescence images of exposed abdomen of healthy nude mice ($N = 2$ for ICG, $N = 3$ for ICB) sacrificed 2 h after retro-orbital injections of either ICG or ICB (10 nmol/mouse). Arbitrary fluorescent unit scale is the same for both images. (b) Representative overlaid brightfield and fluorescence ex vivo images of major organs of nude mice sacrificed 2 h after retro-orbital injection of either ICG or ICB. Fluorescence intensity scale is in arbitrary units. ICB fluorescence image acquired using 700 nm filter; ex: 640/20 nm; em: 710/20 nm; exposure: 3 s; percent power: 50%; F-stop: 2; FOV: 20; binning: low; ICG fluorescence image acquired using 800 nm filter; ex: 810/20 nm; em: 870/20 nm; exposure: 3 s; percent power: 50%; F-stop: 2; FOV: 20; binning: low. (c) Biodistribution of ICG and ICB in nude mice 2 h after dye injection ($N = 2$ for ICG, $N = 3$ for ICB). Error bars represent ± SE. *: $p < 0.05$; **: $p < 0.01$.

Inflammation is associated with changes in micro vascularization and blood vessel permeability, leading to increased accumulation of blood proteins within inflamed tissue. We employed a standard mouse inflammation model that injected lipopolysaccharide (LPS) into a mouse paw and used in vivo fluorescence imaging to visualize blood flow compared to the contralateral paw.[54] More specifically, 50 μL of a solution containing 100 ng of LPS/μL was injected into the right posterior paw to induce inflammation, while a control saline dose was administrated to the left posterior paw (Figure 6a). Two fluorescence imaging paradigms were evaluated. One was a single-agent imaging experiment, where each mouse was given an intravenous injection of either ICB or ICG (100 nmol) and the mouse was imaged over time. Representative mouse fluorescence images are provided in Figures 6b and S14 with a graph in Figure 6c showing the rise and fall in mean pixel intensity for dye fluorescence in each mouse paw over time. The images show significantly higher dye accumulation in the inflamed paw compared to the control paw at 2 h, with extensive dye clearance from both posterior paws by 6 h. The mice were sacrificed at the 6 h time point, and in each case, the exposed abdomen was imaged (Figure S15). The organs were then excised and imaged separately to produce a dye biodistribution profile (Figure S16). As above, there was a much higher background accumulation of ICG in the clearance organs.

The second set of inflammation imaging experiments employed a paired-agent fluorescence imaging paradigm (Figure 6a) that intravenously dosed a mouse with a binary mixture of deep-red ICB and near-infrared ICG (100 nmol each) and employed dual-channel imaging to simultaneously track the location and clearance of each dye (i.e., 700 nm fluorescence channel for ICB and 800 nm fluorescence channel for ICG). Representative mouse fluorescence images are provided in Figures 6d and S17 with a graph in Figure 6e showing the rise and fall of dye fluorescence intensity in each mouse paw over time (see also the ex vivo biodistribution data in Figures S18 and S19). The paired-agent imaging revealed the same trends as the single-agent imaging and demonstrated that the effective perfusion imaging performance of ICG was not altered by the binding of a second dye (ICB) to the blood albumin proteins. In other words, coadministration of ICB did not block albumin binding of ICG, which is not surprising since albumin is a highly abundant blood protein. It is also worth emphasizing that the paired-agent imaging paradigm uses half the number of mice as the single-agent imaging method, but it produces the same conclusions concerning dye localization and biodistribution.[48]

The successful use of deep-red ICB to visualize blood perfusion within a paired-agent imaging experiment prompted us to pursue a more challenging but more clinically relevant paired-agent imaging paradigm, that is, dual-channel imaging of a tumor and its vasculature using a binary admixture of fluorescent probes with different emission wavelengths and targeting properties.[56] We designed a dual-channel imaging experiment that paired ICB, as a deep-red fluorescent probe for visualizing blood perfusion, with a previously reported near-infrared probe called s775cRGD that targets tumor tissue.[48,57] As illustrated in Figure 7a, a tumor mouse model was established with subcutaneously implanted HT-29 cells in the right flank of the mouse. To account for the difference in probe pharmacokinetics, the two probes were administered at different time points. Initially, the mouse was given a retro-orbital injection of tumor targeting s775cRGD (10 nmol), and 3 h later, an injection containing ICB (100 nmol) was delivered retro-orbitally. The living mouse was imaged using filter settings that separately visualized each fluorescent probe (i.e., a 700 nm fluorescence channel for ICB and an 800 nm fluorescence channel for s775cRGD). Shown in Figures 7B and S20 are images at 1 min and 21 h after the ICB administration.

https://doi.org/10.1021/cbmi.4c00008
Chem. Biomed. Imaging 2024, 2, 384−397

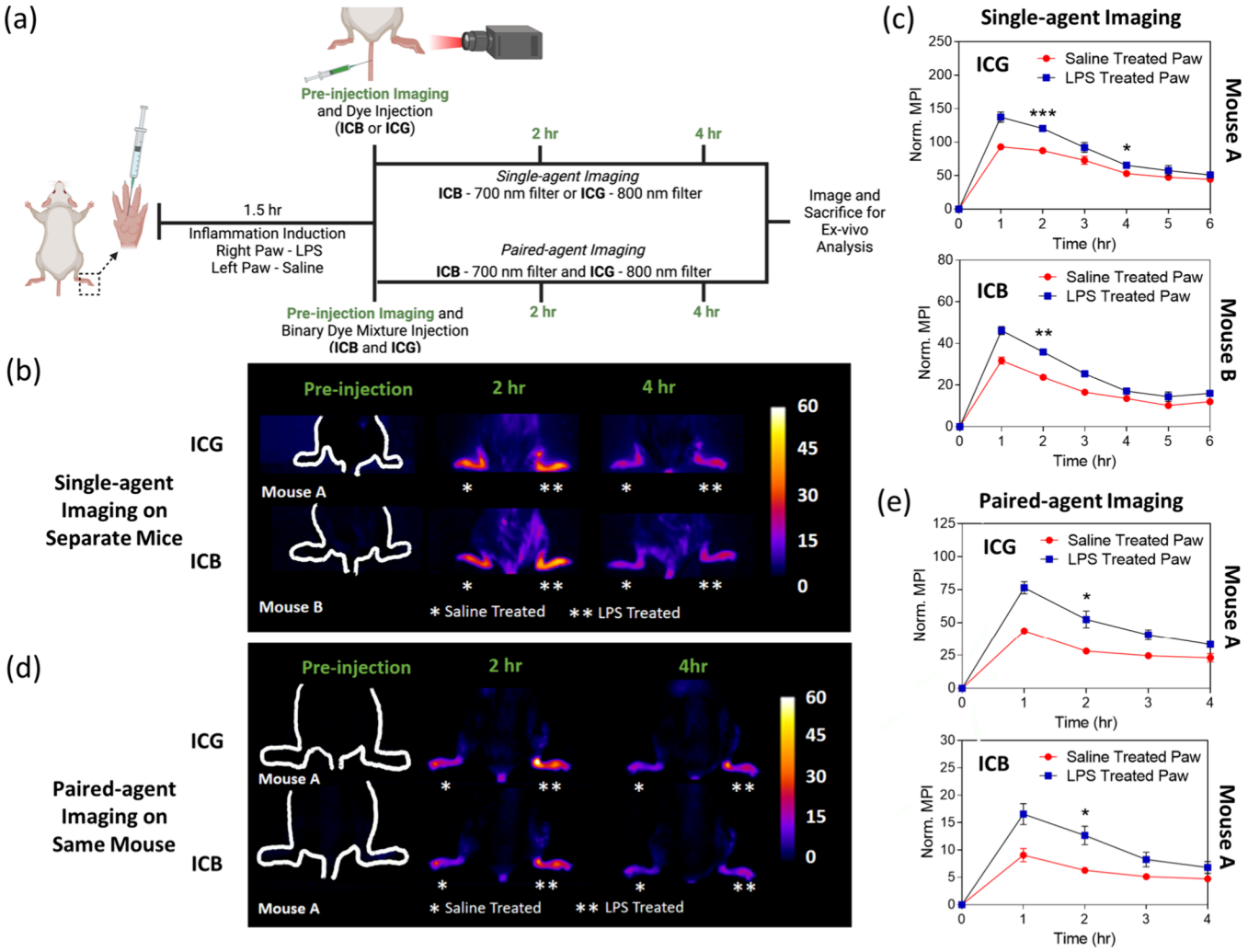

Figure 6. (a) Work-flow for single and paired agent fluorescence imaging of inflamed mouse paw. (b) Representative single agent fluorescence images of inflamed right posterior paw (injected with LPS) and control left posterior paw (injected with saline) for mice (N = 3) imaged at different time points after intravenous dosing with either ICG or ICB (100 nmol dye/mouse). (c) Plots of mean pixel intensity (MPI normalized to preinjection) for mice dosed with ICG or ICB (single agent imaging) at different time points. (d) Representative paired agent fluorescence images of inflamed right posterior paw (injected with LPS) and control left posterior paw (injected with saline) for mice (N = 2) imaged at different time points after intravenous dosing with a binary mixture of ICG and ICB (100 nmol of each dye per mouse). ICB fluorescence image acquired using 700 nm filter; ex: 640/20 nm; em: 710/20 nm; exposure: 3 s; percent power: 50%; F-stop: 2; FOV: 20; binning: medium; ICG fluorescence image acquired using 800 nm filter; ex: 810/20 nm; em: 870/20 nm; exposure: 3 s; percent power: 50%; F-stop: 2; FOV: 20; binning: medium. (e) Plots of normalized MPI for mice dosed with ICG and ICB (paired agent imaging) at different time points. A uniform region of interest was used on each paw to quantify the MPI which then was normalized to t = 0 h for each paw. All calculated MPIs were then adjusted to represent an MPI = 0 at t = 0. Fluorescence intensity scale bar is in arbitrary units. Error bars represent ± SE. *: $p < 0.05$; **: $p < 0.01$; ***: $p < 0.001$ (statistical analyses represent t = 2 h and t = 4 h).

At the 1 min time point, the ICB imaging clearly revealed blood vessels within and around the tumor tissue, but at the 21 h time point, there was no ICB signal due to its rapid and complete clearance from the mouse (see Figures S21 and S22 for additional in vivo and ex vivo imaging data that confirms these conclusions). In contrast, the s775cRGD cleared much more slowly from the mouse, and significant amounts remained in the tumor after 24 h. At that time point, the mouse was sacrificed and the organs were imaged to determine a final biodistribution (Figure S22). As expected, ICB cleared through the liver and s775cRGD, through the kidneys.[48,57] This proof-of-concept study highlights the great potential of utilizing deep-red ICB for rapid visualization of the vasculature within cancerous tissue that has been simultaneously stained using cancer targeting near-infrared s775cRGD.[56] Preclinical research studies could use this information to assess how microvascular permeability changes with tumor physiology or experimental therapy.[58] Ultimately, it could be incorporated into clinical protocols that determine patient response to treatments that are designed to alter tumor perfusion.[59] In this regard, improved pharmacokinetic insight is gained by using fluorescent agents with varied sizes since they will be sensitive to different hemodynamic regimes. Since ICB binds strongly to albumin, its effective diameter is the size of the 67 kDa protein. In recent years, several hydrophilic near-infrared fluorophores have been developed with negligible albumin affinity and much smaller hydrodynamic diameters than an ICB/albumin complex.[17,60] This suggests new classes of dynamic contrast enhanced imaging methods can be developed based on the paired agent imaging paradigm.[61,62]

https://doi.org/10.1021/cbmi.4c00008
Chem. Biomed. Imaging 2024, 2, 384−397

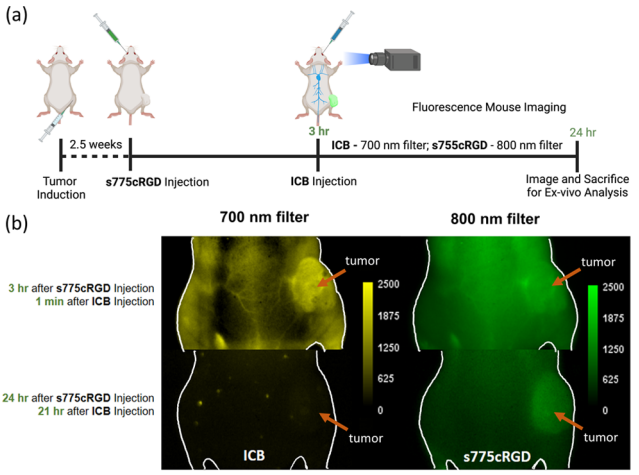

Figure 7. (a) Work-flow for dual-channel imaging of mouse vasculature. (b) Dual-channel fluorescence images of a tumor bearing nude mouse at two different time points after retro-orbital injection of s775cRGD (10 nmol/mouse) experiment time zero and retro-orbital injection of ICB (100 nmol/mouse) three hours later. ICB fluorescence image acquired using 700 nm filter; ex: 640/20 nm; em: 710/20 nm; exposure: 3 s; percent power: 50%; F-stop: 2; FOV: 20; binning: low; s775cRGD fluorescence image acquired using 800 nm filter; ex: 745/20 nm; em: 850/20 nm; exposure: 3 s; percent power: 50%; F-stop: 2; FOV: 20; binning: low. Fluorescence intensity scales are in arbitrary units.

CONCLUSIONS

The heptamethine cyanine dye, ICG, is by far the most used near-infrared fluorescent dye in biomedicine. ICB, the homologous pentamethine cyanine dye with a deleted vinylidene unit, exhibits the expected spectral differences (Table 1) including absorption/emission maxima peaks at a 100 nm lower wavelength. Compared to ICG, ICB is >1000-fold more hydrophilic but still has high affinity for albumin protein. These specific spectral and physicochemical differences enable the design of comparative experiments that test fundamental hypotheses in fluorescence-based research. The strategy was incorporated into a spectroscopy study that tested a recently proposed FRET mechanism for enhanced dye fluorescence brightness in heavy water (D_2O). A switch from H_2O to D_2O increased the fluorescence brightness for near-infrared ICG by a factor of 2.94, which was significantly more than the increase of 1.56 determined for deep-red ICB. This trend is consistent with a FRET-based quenching pathway and increased spectral overlap of the ICG emission band with high energy O−H absorption bands in the region of 700−900 nm. It is increasingly clear that the heavy water fluorescence enhancement effect will be most useful for microscopy or imaging when the fluorophore emits near-infrared wavelengths above 650 nm. However, there is a notable caveat: the heavy water florescence enhancement effect for an amphiphilic near-infrared cyanine dye, like ICG, is substantially diminished if the dye is bound by albumin protein. In this scenario, the surface of the albumin-bound dye is partially dehydrated, which lowers the efficiency of fluorescence quenching by FRET to H_2O and diminishes the magnitude of the heavy water florescence enhancement effect. Thus, to ensure a large heavy water florescence enhancement effect, it is crucial to employ a hydrophilic near-infrared dye that has emission >650 nm and negligible affinity for proteins or membranes. During these studies, we observed that ICG fluorescence in D_2O is decreased by 30% upon binding to BSA. This finding is extraordinary because enhancement of dye fluorescence upon binding to albumin in H_2O is a universal phenomenon. We suggest that researchers consider dye-binding experiments in D_2O as a simple way to mask the extensive fluorescence quenching by H_2O and uncover more subtle alternative dye excited state relaxation pathways.

A combination of cell microscopy and mouse biodistribution studies found that ICB and ICG interact with proteins and cells in very similar ways. However, there are some small but meaningful pharmacokinetic differences. ICB rapidly transports through the mouse liver into the intestines with significantly lower background tissue retention than ICG. Mouse fluorescence imaging studies demonstrated the potential utility of ICB for dual-channel, paired agent imaging in a living subject. One set of imaging experiments visualized increased blood flow in a mouse model of inflamed tissue, and a second set of mouse tumor imaging experiments simultaneously visualized the vasculature and cancerous tissue in separate fluorescence channels. Cancer imaging studies can use this paired agent imaging information to assess how microvascular permeability changes with tumor physiology or experimental therapy.

EXPERIMENTAL SECTION

General

The chemical name of ICB is (2-[5-[1,1-dimethyl-3-(4-sulfobutyl)-1,3-dihydro-benzo[e]indol-2-ylidene]-penta-1,3-dienyl]-1,1-dimethyl-3-(4-sulfobutyl)-1*H*-benzo[e]indoliumhydroxide, inner salt, sodium salt), and it was purchased from TCI America. Indocyanine Green (ICG) was purchased from Sigma-Aldrich. High dye purity was confirmed by NMR spectroscopy recorded on a Bruker 500 NMR spectrometer. Additional evidence for high dye purity was gained by showing that the dye excitation spectrum matched the dye absorption spectrum. Absorption spectra were recorded on an Evolution 201 UV/vis spectrometer with Thermo Insight software. Fluorescence spectra were collected on a Horiba Fluoromax plus c fluorometer with FluoroEssence software.

Fluorescence Quantum Yield

Quantum yield measurement of ICB used Methylene Blue (ϕ_F = 2.0% in water) as a reference standard. The concentrations of Methylene Blue and ICB were adjusted to an absorbance value of 0.065 at 620 nm. The fluorescence spectrum of each dye in H_2O was obtained with excitation at 620 nm, with a slit width of 3 nm, and the integrated area was used in the quantum yield calculation by the following equation: where η is the refractive index of the solvent, I is the integrated fluorescence intensity, and A is the absorbance at a chosen excitation wavelength. The measurement was conducted in triplicate with the reported quantum yield corresponding to the mean value ± standard deviation.

$$\varnothing_{sample} = \varnothing_{ref} \times \frac{\eta_{sample}{}^2 I_{sample} A_{sample}}{\eta_{ref}{}^2 I_{ref} A_{ref}}$$

Fluorescence Excited State Lifetime

Fluorescence decay of ICG and ICB was recorded using time-correlated signal photon counting (TCSPC) using a Horiba Jobin Yvon system that was connected to an IBH Data Station Hub for timing. Dye concentration was 5 μM in DMSO or PBS, at pH 7.4, and measurements were obtained at room temperature. Dyes were excited using a 375 nm Nano LED (Horiba Scientific Inc.). Emission for ICB was collected at 700 nm and that for ICG, at 800 nm. The decay profiles for ICB were treated as monoexponentials, but the ICG profiles exhibited a biexponential trend as the photoluminescence decay of ICG in PBS, pH 7.4, and H_2O was closer to the instrument

https://doi.org/10.1021/cbmi.4c00008
Chem. Biomed. Imaging 2024, 2, 384−397

response function (IRF) of the time-correlated single photon counting setup.

Fluorescent Enhancement in D_2O and BSA Effect

Spectroscopy Study. Emission spectra for ICB and ICG (1 μM) were obtained at room temperature in H_2O or D_2O (ICB ex: 650 nm; ICG ex: 750 nm) samples with 3 nm slit width. Some samples were supplemented with BSA (500 μM). Integrated Fluorescence (I.F.) was collected for ICB (660−803 nm) or ICG (760−885 nm).

***In Vivo* Imaging Station Study.** The fluorescence intensity of ICB or ICG in D_2O or H_2O was measured by using a 96-well plate imaging assay. Solutions of each dye (1 μM) were prepared with different volume ratios of D_2O in H_2O (0−100% D_2O). Fluorescence images of duplicates were obtained in a black 96-well plate by using a commercial in vivo imaging station (Ami HT Spectral Imaging). ICB fluorescence images acquired using a 700 nm filter; ex: 640/20 nm; em: 710/20 nm; exposure: 3 s; percent power: 50%; F-stop: 2; FOV: 20; binning: low; ICG fluorescence images acquired using an 800 nm filter; ex: 810/20 nm; em: 870/20 nm; exposure: 3 s; percent power: 50%; F-stop: 2; FOV: 20; binning: low. Some samples were supplemented with BSA (500 μM). Mean pixel intensity maps of the images were obtained using ImageJ software and were normalized to the highest mean pixel intensity of the samples.

Solvent-Dependent Aggregation

Concentration-dependent dye aggregation of ICB and ICG in three different solvents, H_2O, D_2O, and PBS, pH 7.4, was studied by varying the dye concentration from 1 to 10 μM. Both absorption and emission spectra for each condition were recorded at room temperature. Excitation wavelengths were ICB ex: 650 nm and ICG ex: 750 nm, with 3 nm slit width.

1-Octanol/Buffer Partitioning

Samples were prepared in 1 mL Eppendorf tubes using equal volumes of 1-octanol and HEPES buffer (50 mM HEPES, 100 mM NaCl, pH 7.4) or HEPES buffer containing BSA (0.25 mM). An aliquot of ICB or ICG (10 μM) was pipetted into the 1-octanol layer, and the biphasic mixture was vigorously shaken for 15 s and then centrifuged at 1000g for 2 min to cleanly separate the two phases. A 250 μL aliquot from each phase was transferred to a 96-well plate, and the absorbance at 780 nm for ICG or 680 nm for ICB was recorded. Log P was determined using the formula $P = \log(A_{octanol}/A_{buffer})$ where $A_{octanol}$ = absorbance of dye in octanol phase and A_{buffer} = absorbance of dye in buffer phase at the relevant wavelength. All measurements were performed in triplicate.

ICB Stability (Storage, Photo-, and Thermal)

Aliquots (1.0 mL) were taken from a room temperature stock solution (1.0 mM, 20 mL) of ICB in water at different time points (sample exposed to lab lights only during preparation and when aliquots were removed). At each time point, the 1.0 mL aliquot was lyophilized, and the solid residue was dissolved in 0.60 mL of methanol-d_4 to permit ^{1}H NMR (500 MHz) analysis. To measure the photostability, two separate cuvettes, each containing 1 μM of ICB or ICG in PBS buffer, pH 7.4, were irradiated at a set 3 cm distance by using a 150 W xenon lamp (Oreal Corporation, USA) equipped with a 620 nm long-pass filter (Edmunds Optics Inc., USA). ICB thermal stability was assessed by irradiating a 5 μM dye in PBS buffer, pH 7.4, with a 640 nm continuous laser (Coherent OBIS 640, Edmunds Optics, USA) for 10 min under a power intensity of 1 mW/cm^2. Temperature was recorded using an infrared camera (Infrared Cameras Inc., 7320). Dye fatigue was recorded by conducting five, 10 min heating/cooling cycles. The experiment was repeated in triplicate. and averaged thermal cycles were reported.

Bovine Serum Albumin Binding

Approximate albumin association constants were determined by conducting a titration procedure that added aliquots of ICB (or ICG) to a solution of BSA (Sigma-Aldrich A964) and monitored quenching of fluorescence from the single tryptophan in the BSA (excitation: 280 nm; slit width: 2 nm). The fluorescent change ΔF was calculated using the equation $(F_0 - F)$ where F_0 = initial fluorescence intensity and F = fluorescent intensity after each aliquot addition. The approximate dissociation constant (K_d) was determined using GraphPad Prism by fitting the dye concentration-dependent ΔF plot to a nonlinear one site-specific binding model.[63] Validation experiments showed that light absorption by the added dye at the tryptophan excitation wavelength (280 nm) was negligible before albumin saturation (Figure S4), and it was assumed to not significantly reduce tryptophan emission enough to alter the titration profile.

Dye Stability in Serum

A 96 well plate was loaded with solutions containing ICG or ICB at concentrations ranging from 0 to 100 μM in PBS buffer (pH 7.4) containing either 0.1% mouse serum or human serum. Fluorescence images of each plate were acquired at t = 0, 1, and 2 h. Fluorescence images acquired using 700 nm filter; ex: 640/20 nm; em: 710/20 nm; exposure: 3 s; percent power: 50%; F-stop: 2; FOV: 20; binning: low; ICG fluorescence images acquired using 800 nm filter; ex: 810/20 nm; em: 870/20 nm; exposure: 3 s; percent power: 50%; F-stop: 2; FOV: 20; binning: low. The mean pixel intensity of each well in an image was determined using ImageJ2 software and normalized to the value for the well containing 100 μM dye at 0 h.

MTT Cell Metabolic Activity Assay[64]

HT-29 (human colorectal adenocarcinoma), A549 (lung carcinoma epithelial), and U87 (human glioblastoma) were acquired from ATCC. The HT-29 cells were cultured in McCoy's 5A medium (supplemented with 10% fetal bovine serum and 1% penicillin/streptomycin) at 37 °C and 5% CO_2 in a humidified incubator. The A549 cells were cultured in F-12K medium (supplemented with 10% fetal bovine serum and 1% penicillin−streptomycin) at 37 °C and 5% CO_2 in a humidified incubator. The U87 cells were cultured in DMEM medium (supplemented with 10% fetal bovine serum and 1% penicillin/streptomycin) at 37 °C and 5% CO_2 in a humidified incubator. In each case, cells were seeded into 96-microwell plates and grown to 80% confluency. The medium was then removed and replaced with ICB at various micromolar concentrations (N = 3) in the respective medium for 24 h at 37 °C and 5% CO_2 in a humidified incubator. After 24 h, the dye was removed and replaced with growth medium containing [3-(4,5-dimethylthiazol-2-yl)-2,5-diphenyltetrazolium bromide] (MTT, 1.1 mM). After a 4 h incubation at 37 °C and 5% CO_2, SDS-DMSO detergent solution was added to the cells. The samples were incubated overnight, and the absorbance of each well was measured at 590 nm. The readings were normalized to those of untreated cells for each dye. All data are the average of triplicate measurements.

Dye Uptake by Cells

HT-29 cells were seeded and grown to 70% confluency on 8-well plates (Lab-Tek, USA). The cells were incubated with 5 μM ICB in media for 2 h at either 37 or 4 °C and 5% CO_2 in a humidified incubator. Next, the cells were washed twice with 1× PBS cells and stained with 3 μM Hoechst 33342 for 10 min. After a single wash of 1× PBS, the live cells were imaged in Opti-MEM using a Zeiss Axiovert 100 TV epifluorescence microscope under a UV filter (ex: 387/11; em: 447/60) and Cy5.5 filter (ex: 635/40; em: 696/40). For each micrograph, a background subtraction with a rolling ball radius of 50 pixels was applied using ImageJ2 software. After calculating the average mean pixel intensity (MPI) for each micrograph, GraphPad Prism was used to plot the data. For each condition, a total of nine micrographs were analyzed. The experiments were conducted in triplicate.

Studies of inhibition of the organic anion transporter used HT-29 cells that were seeded and grown to 70% confluency on 35 mm × 10 mm clear wall glass bottom dishes (Pelco, USA). Inhibition of the organic anion transporter was achieved by preincubating cells with 100 μM sulfobromopthalein (BSP) in media for 1 h at 37 °C and 5% CO_2 in a humidified incubator. A control batch of cells was not treated with BSP. After two washes with 1× PBS, both batches of cells were incubated with 5 μM ICB in media for 2 h at 37 °C and 5% CO_2 in a humidified incubator. Next, the cells were washed twice with 1×

https://doi.org/10.1021/cbmi.4c00008
Chem. Biomed. Imaging 2024, 2, 384−397

PBS and fixed with 4% cold paraformaldehyde for 20 min at room temperature. After a single wash with 1× PBS, the cells were costained with 3 μM Hoechst 33342 for 10 min. After a single wash of 1× PBS, the cells were imaged using a Keyence BZ-X810 fluorescence microscope using a UV filter (ex: 387/11; em: 447/60) and Cy5 filter (ex: 604/40; em: 672/50). For each micrograph, a background subtraction with a rolling ball radius of 100 pixels was applied using ImageJ2 software. After calculating the average MPI for each micrograph, GraphPad Prism was used to plot the data. For each condition, a total of six micrographs were analyzed. The experiments were conducted in triplicate.

Dye Localization in Cells

To study the cellular localization of ICB, HT29 cells were seeded and grown to 70% confluency on 35 mm × 10 mm clear wall glass bottom dishes (Pelco, USA). The cells were then incubated with 5 μM ICB in media for either 2 or 24 h at 37 °C and 5% CO_2 in a humidified incubator. At the end of ICB incubation, cells were washed twice with 1× PBS and incubated with 1 μM MitoTracker Red or LysoTracker Red for 15 min at 37 °C and 5% CO_2 in a humidified incubator. Next, the cells were washed twice with 1× PBS and fixed with 4% cold paraformaldehyde for 20 min at room temperature. After a single wash with 1× PBS, the cells were costained with 3 μM Hoechst 33342 for 10 min. After a single wash of 1× PBS, cells were imaged using a Keyence BZ-X810 fluorescence microscope using a UV filter (ex: 387/11; em: 447/60), Cy5 filter (ex: 604/40; em: 672/50), and TxRd filter (ex: 559/34; em: 639/69). For each micrograph, a background subtraction with a rolling ball radius of 100 pixels was applied using ImageJ2 software. The colocalization of ICB with the trackers at each time point was determined by measuring the Pearson Correlation Coefficients using ImageJ2 software. The experiments were conducted in triplicate.

Dye Brightness in Intralipid Phantom

Phantom study used a capillary tube containing 50 μM ICB in FBS at penetration depths of 0−5 mm in 1% intralipid. Images acquired using Ami HT in vivo imaging station with 700 filter; ex: 640/20 nm; em: 710/20 nm; exposure: 3 s; percent power: 50%; F-stop: 2; FOV: 20; binning: low. Mean pixel intensity of a constant ROI on the capillary tube was quantified and corrected to account for the background by subtracting the mean pixel intensity of an ROI from 1% intralipid. Signals were normalized to the corrected MPI at 0 mm. The experiment was duplicated.

Biodistribution in Healthy Mice

All in vivo mouse experiments followed a protocol that was approved by the Notre Dame Institutional Animal Care and Use Committee. Ten month old healthy female Foxn1 mice were given a retro-orbital injection of either ICG or ICB (N = 2 for ICG, N = 3 for ICB,100 μL, 10 nmol/mouse). At 2 h, the mice were anesthetized and sacrificed by cervical dislocation followed by the immediate collection of blood from the heart. The abdominal cavity was exposed, and the mice were imaged using a commercial in vivo imaging station (Ami HT Spectral Imaging). ICB fluorescence images acquired using 700 nm filter; ex: 640/20 nm; em: 710/20 nm; exposure: 3 s; percent power: 50%; F-stop: 2; FOV: 20; binning: low; ICG fluorescence images acquired using 800 nm filter; ex: 810/20 nm; em: 870/20 nm; exposure: 3 s; percent power: 50%; F-stop: 2; FOV: 20; binning: low. For image processing, the mouse body images were colored "fire" using ImageJ2 software. After abdominal cavity images were obtained, the major organs were harvested and imaged on a transparent plastic tray using the in vivo imaging station. For the biodistribution analysis of each excised organ, images were imported to ImageJ2, and a manually drawn region of interest was created around each organ. Mean Pixel Intensity (MPI) of each organ was divided by the MPI of the thigh muscle from the same mouse to give a normalized MPI for each dye to compare the fate of the dye after 2 h.

Imaging Mouse Paw Inflammation Model

Jackson lab BALB/c female mice weighing >20 g were used for the procedure. A chemically induced paw inflammation model was established using the following steps developed based on the literature.[54] Lipopolysaccharide (LPS) from *Escherichia coli* was used as an inflammation stimulator. Mice (N = 6) were placed under anesthesia (1.5 L O_2/min, 2.0% isoflurane) in a prone position to facilitate intraplantar administration. To induce inflammation, 50 μL of 100 ng of LPS/μL stock solution was injected using a 30-gauge needle into the right posterior paw, while 50 μL of sterile saline was administered to the left posterior paw as a control. Following the injections, mice were monitored in their cages for 1.5 h with an adequate supply of water and food. At 1.5 h postinjection, swelling of the inflamed foot was apparent, and the single agent imaging experiments were administered intravenously through a tail-vein injection under anesthesia of 100 μL of ICG or ICB (100 nmol/mouse, each dye N = 3). Each mouse was imaged by using a commercial in vivo imaging station (Ami HT Spectral Imaging). ICB fluorescence images were acquired using 700 nm filter; ex: 640/20 nm; em: 710/20 nm; exposure: 3 s; percent power: 50%; F-stop: 2; FOV: 20; binning: medium; ICG fluorescence images were acquired using 800 nm filter; ex: 810/20 nm; em: 870/20 nm; exposure: 3 s; percent power: 50%; F-stop: 2; FOV: 20; binning: medium at 0, 1, 2, 3, 4, 5, and 6 h time points. Dye fluorescence in the living mouse paws was calculated at each time point by analyzing the MPI of a region of interest (ROI) drawn around the right posterior paw or the left posterior paw of equal size. At 6 h, the mice were anesthetized and sacrificed by cervical dislocation followed by the immediate collection of blood from the heart. The exposed mouse cavity was revealed and imaged. The liver, lungs, heart, spleen, intestine, stomach, pancreas, kidneys, skin, muscles, and both paws were harvested and imaged on a transparent plastic tray. For image processing, the mouse body images were colored "fire" using ImageJ2 software. The images of excised organs were imported into ImageJ2, and a manually drawn region of interest was created around each organ. Mean Pixel Intensity (MPI) of each organ was divided by the MPI of the thigh muscle from the same mouse to give a normalized MPI for each dye.

For the paired agent imaging experiments, the same procedure was used to induce inflammation with N = 2 mice. At 1.5 h after the LPS and saline treatments, each mouse was injected with a 100 μL dose containing a binary mixture of ICG and ICB (200 nmol/mouse, 100 nmol of each dye). Each mouse was imaged using the ICG and ICB filter settings described above with a 1 s interval between the image capture at 0, 1, 2, 3, and 4 h. At 4 h, the mice were anesthetized and sacrificed by cervical dislocation, and imaging was used to ascertain biodistribution and to quantify dye accumulation in the inflamed tissue.

Multicolor Perfusion and Biodistribution Imaging in Tumor Mouse Model

A female Foxn1 nude mouse was injected in the right flank with a mixture of HT-29 colorectal adenocarcinoma (5 × 10^6 cells) and matrigel (1:1), and 3 weeks later, a subcutaneous tumor had developed. Five minutes before the fluorescent probe injection procedure, the mouse was placed under 2−3% isoflurane anesthesia and imaged using two fluorescence filter channels, the 700 nm filter for the ICB; ex: 640/20 nm; em: 710/20 nm; exposure: 3 s; percent power: 50%; F-stop: 2; FOV: 20; binning: low; 800 nm filter for targeted s775cRGD probe; ex: 745/20 nm; em: 850/20 nm; exposure: 3 s; percent power: 50%; F-stop: 2; FOV: 20 or 10; binning: low, using an in vivo imaging station (Ami HT Spectral Imaging). After mouse retro-orbital injection with a 100 μL dose of the targeted probe s775cRGD (10 nmol/mouse) in saline, the mouse was imaged at 0, 1, 2, and 3 h time points. The tumor-to-background ratio for each living mouse image was calculated at each time point by analyzing the MPI of a region of interest (ROI) drawn around the tumor or the opposite flank in equal size. After three hours, a 100 μL dose of the ICB (100 nmol/mouse) was injected via the tail vein and the mouse was imaged at 0, 1 min, 5 min, 10 min, and 1, 2, 3, and 21 h post-injection under 700 and 800 nm filter settings. At 24 h post-injection of s775cRGD, the mouse was anesthetized and sacrificed by cervical dislocation followed by immediate collection of blood from the heart. The whole mouse was imaged with the tumor exposed by

https://doi.org/10.1021/cbmi.4c00008
Chem. Biomed. Imaging 2024, 2, 384−397

removing the surrounding skin and, then, after excising the tumor from the body. Next, the liver, lungs, heart, spleen, intestine, pancreas, kidneys, skin, and muscles were harvested. The excised tumors and organs were imaged on a transparent plastic tray. For image processing, the mouse body and the excised tumor images were false-colored "yellow" for 700 nm filter and "green" for 800 nm filter using ImageJ2 software. An arbitrary maximum fluorescence value was chosen for the analysis. For the biodistribution and ex vivo tumor analyses, the images of excised tumor and organs were imported to ImageJ2, and a manually drawn ROI was created around each fluorescent image. The MPI of each tumor or organ was divided by the MPI of the thigh muscle from the same mouse to give a normalized MPI.

■ ASSOCIATED CONTENT

Supporting Information

The Supporting Information is available free of charge at https://pubs.acs.org/doi/10.1021/cbmi.4c00008.

Experimental procedures, chemical and photophysical data, cell metabolic activity, cell microscopy of ICB localization, expansion of mouse biodistribution data, inflammation imaging, and multicolor perfusion and biodistribution imaging data (PDF)

■ AUTHOR INFORMATION

Corresponding Author

Bradley D. Smith − *Department of Chemistry and Biochemistry, University of Notre Dame, Notre Dame, Indiana 46556, United States;* orcid.org/0000-0003-4120-3210; Email: smith.115@nd.edu

Author

Rananjaya S. Gamage − *Department of Chemistry and Biochemistry, University of Notre Dame, Notre Dame, Indiana 46556, United States;* orcid.org/0000-0003-3960-0276

Complete contact information is available at: https://pubs.acs.org/10.1021/cbmi.4c00008

Notes

The authors declare no competing financial interest.

■ ACKNOWLEDGMENTS

The authors are grateful for funding support from the US NIH (R35GM136212). We thank Zhumin Zhang for measuring dye storage stability and Jishnudas Chakkamalayath for fluorescence lifetime measurements. All graphical representations were created with BioRender.com.

■ ABBREVIATIONS

ICB, Indocyanine Blue
ICG, Indocyanine Green
FRET, Förster Resonance Energy Transfer
H_2O, Light Water
D_2O, Heavy Water
BSA, Bovine Serum Albumin
LPS, Lipopolysaccharide
SD, Standard Deviation
SEM, Standard Error of Mean
SDS, Sodium Dodecyl Sulfonate
DMSO, Dimethyl Sulfoxide

■ REFERENCES

(1) Reinhart, M. B.; Huntington, C. R.; Blair, L. J.; Heniford, B. T.; Augenstein, V. A. Indocyanine Green :Historical Context, Current Applications, and Future Considerations. *Surg. Innov.* **2016**, *23*, 166−175.

(2) Levesque, E.; Martin, E.; Dudau, D.; Lim, C.; Dhonneur, G.; Azoulay, D. Current Use and Perspective of Indocyanine Green Clearance in Liver Diseases. *Anaesth. Crit. Care Pain Med.* **2016**, *35*, 49−57.

(3) Desmettre, T.; Devoisselle, J. M.; Mordon, S. Fluorescence Properties and Metabolic Features of Indocyanine Green (ICG) as Related to Angiography. *Surv. Ophthalmol.* **2000**, *45*, 15−27.

(4) Fanaropoulou, N. M.; Chorti, A.; Markakis, M.; Papaioannou, M.; Michalopoulos, A.; Papavramidis, T. The Use of Indocyanine Green in Endocrine Surgery of the Neck. *Medicine* **2019**, *98*, No. e14765.

(5) Peltrini, R.; Podda, M.; Castiglioni, S.; Di Nuzzo, M. M.; D'Ambra, M.; Lionetti, R.; Sodo, M.; Luglio, G.; Mucilli, F.; Di Saverio, S.; et al. Intraoperative Use of Indocyanine Green Fluorescence Imaging in Rectal Cancer Surgery: The State of the Art. *World J. Gastroentero* **2021**, *27*, 6374−6386.

(6) Wilke, B. K.; Schultz, D. S.; Huayllani, M. T.; Boczar, D.; Spaulding, A. C.; Sherman, C.; Murray, P.; Forte, A. J. A Prospective Evaluation of Intraoperative Indocyanine Green Fluorescence Angiography for Soft Tissue Sarcomas. *J. Am. Acad. Orthop. Surg. Glob. Res. Rev.* **2021**, *5*, e21.00187-6.

(7) Maarek, J. M. I.; Holschneider, D. P.; Harimoto, J. Fluorescence of Indocyanine Green in Blood: Intensity Dependence on Concentration and Stabilization with Sodium Polyaspartate. *J. Photoch. Photobio. B* **2001**, *65*, 157−164.

(8) Cosco, E. D.; Lim, I.; Sletten, E. M. Photophysical Properties of Indocyanine Green in the Shortwave Infrared Region. *ChemPhotoChem.* **2021**, *5*, 727−734.

(9) Li, D.-H.; Smith, B. D. Deuterated Indocyanine Green (ICG) with Extended Aqueous Storage Shelf-Life: Chemical and Clinical Implications. *Chem. − Eur. J.* **2021**, *27*, 14535−14542.

(10) Gerega, A.; Zolek, N.; Soltysinski, T.; Milej, D.; Sawosz, P.; Toczylowska, B.; Liebert, A. Wavelength-Resolved Measurements of Fluorescence Lifetime of Indocyanine Green. *J. Biomed. Opt.* **2011**, *16*, No. 067010.

(11) Gowsalya, K.; Yasothamani, V.; Vivek, R. Emerging Indocyanine Green-Integrated Nanocarriers for Multimodal Cancer Therapy: A Review. *Nanoscale Adv.* **2021**, *3*, 3332−3352.

(12) Tan, A. C. S.; Fleckenstein, M.; Schmitz-Valckenberg, S.; Holz, F. G. Clinical Application of Multicolor Imaging Technology. *Ophthalmologica* **2016**, *236*, 8−18.

(13) Tan, C. S.; Ting, D. S.; Lim, L. W. Multicolor Fundus Imaging of Polypoidal Choroidal Vasculopathy. *Ophthalmol. Retina* **2019**, *3*, 400−409.

(14) Wu, M.-R.; Huang, Y.-Y.; Hsiao, J.-K. Use of Indocyanine Green (ICG), a Medical Near Infrared Dye, for Enhanced Fluorescent Imaging—Comparison of Organic Anion Transporting Polypeptide 1B3 (OATP1B3) and Sodium-Taurocholate Cotransporting Polypeptide (NTCP) Reporter Genes. *Molecules* **2019**, *24*, 2295.

(15) Kumar, A. T. N.; Carp, S. A.; Yang, J.; Ross, A.; Medarova, Z.; Ran, C. Fluorescence Lifetime-Based Contrast Enhancement of Indocyanine Green-Labeled Tumors. *J. Biomed. Opt.* **2017**, *22*, No. 040501.

(16) Corcione, F.; Silvestri, V.; Merola, G.; Dambra, M.; Lionetti, R.; Pirozzi, N.; Peltrini, R.; Pontecorvi, E.; Bracale, U. Use of the ORBEYE^{TM} Exoscope in General Surgery: The Advent of Video-Assisted Open Surgery. *Surg. Innov.* **2021**, *28*, 79−84.

(17) Li, D. H.; Gamage, R. S.; Smith, B. D. Sterically Shielded Hydrophilic Analogs of Indocyanine Green. *J. Org. Chem.* **2022**, *87*, 11593−11601.

(18) Chapman, G.; Henary, M.; Patonay, G. The Effect of Varying Short-Chain Alkyl Substitution on the Molar Absorptivity and Quantum Yield of Cyanine Dyes. *Anal. Chem. Insights* **2011**, *6*, 29−36.

(19) Karlsson, J. K. G.; Woodford, O. J.; Mustroph, H.; Harriman, A. Cyanine Dyes as Ratiometric Fluorescence Standards for the Far-Red Spectral Region. *Photoch. Photobio. Sci.* **2018**, *17*, 99−106.
(20) v. Berlepsch, H.; Bottcher, C. H-Aggregates of an Indocyanine Cy5 Dye: Transition from Strong to Weak Molecular Coupling. *J. Phys. Chem. B* **2015**, *119*, 11900−11909.
(21) Hochheimer, B. F. A Dye for Experimental Choroidal Angiography. *Exp. Eye Res.* **1979**, *29*, 141−143.
(22) Mustroph, H. Cyanine Dyes. *Phys. Sci. Rev.* **2020**, *5*, 1−24.
(23) Lee, S.-K.; Mills, A. Luminescence of Leuco-Thiazine Dyes. *J. Fluoresc.* **2003**, *13*, 375−377.
(24) Tatikolov, A. S.; Costa, S. M. B. Complexation of Polymethine Dyes with Human Serum Albumin: A Spectroscopic Study. *Biophys. Chem.* **2004**, *107*, 33−49.
(25) Jung, B.; Vullev, V. I.; Anvari, B. Revisiting Indocyanine Green: Effects of Serum and Physiological Temperature on Absorption and Fluorescence Characteristics. *IEEE J. Sel. Top. Quant.* **2014**, *20*, 149−157.
(26) Gamage, R. S.; Smith, B. D. Spontaneous Transfer of Indocyanine Green from Liposomes to Albumin Is Inhibited by the Antioxidant α-Tocopherol. *Langmuir* **2022**, *38*, 11950−11961.
(27) Berezin, M. Y.; Lee, H.; Akers, W.; Achilefu, S. Near Infrared Dyes as Lifetime Solvatochromic Probes for Micropolarity Measurements of Biological Systems. *Biophys. J.* **2007**, *93*, 2892−2899.
(28) Fang, X.; Liu, W.; Wu, X.; Zhou, W.; Chen, J.; Liu, X.; Xu, Z. One-Step Condensation Synthesis and Characterizations of Indocyanine Green. *Results Chem.* **2021**, *3*, No. 100092.
(29) Henary, M.; Mojzych, M. Stability and Reactivity of Polymethine Dyes in Solution. In *Heterocyclic Polymethine Dyes*; Strekowski, L., Ed.; Springer, 2008; pp 221−238; DOI: 10.1007/7081_2008_111.
(30) Sens, R.; Drexhage, K. H. Fluorescence Quantum Yield of Oxazine and Carbazine Laser Dyes. *J. Lumin.* **1981**, *24*−*25*, 709−712.
(31) Kučera, J.; Peš, O.; Janovič, T.; Hofr, C.; Kubinyiová, L.; Tóth, J.; Káňa, Š.; Táborský, P. Enhancement of Luminescence Signal by Deuterated Water − Practical Implications. *Sensor. Actuat. B-Chem.* **2022**, *352*, No. 131029.
(32) Klehs, K.; Spahn, C.; Endesfelder, U.; Lee, S. F.; Fürstenberg, A.; Heilemann, M. Increasing the Brightness of Cyanine Fluorophores for Single-Molecule and Superresolution Imaging. *ChemPhysChem* **2014**, *15*, 637−641.
(33) Ong, W. Q.; Citron, Y. R.; Schnitzbauer, J.; Kamiyama, D.; Huang, B. Heavy Water: A Simple Solution to Increasing the Brightness of Fluorescent Proteins in Super-Resolution Imaging. *Chem. Commun.* **2015**, *51*, 13451−13453.
(34) Dobretsov, G. E.; Syrejschikova, T. I.; Smolina, N. V. On Mechanisms of Fluorescence Quenching by Water. *Biophysics-USSR* **2014**, *59*, 183−188.
(35) Maillard, J.; Klehs, K.; Rumble, C.; Vauthey, E.; Heilemann, M.; Fürstenberg, A. Universal Quenching of Common Fluorescent Probes by Water and Alcohols. *Chem. Sci.* **2021**, *12*, 1352−1362.
(36) Maillard, J.; Rumble, C. A.; Fürstenberg, A. Red-Emitting Fluorophores as Local Water-Sensing Probes. *J. Phys. Chem. B* **2021**, *125*, 9727−9737.
(37) Matikonda, S. S.; Hammersley, G.; Kumari, N.; Grabenhorst, L.; Glembockyte, V.; Tinnefeld, P.; Ivanic, J.; Levitus, M.; Schnermann, M. J. Impact of Cyanine Conformational Restraint in the Near-Infrared Range. *J. Org. Chem.* **2020**, *85*, 5907−5915.
(38) Jiang, G.; Hu, Z.; Bai, L.; Zhong, C.; Lu, S.; Han, B.; Sun, Z.; Zhu, S.; Liang, Y.; Sun, H. Origins of Near-Infrared-II Emission Tail and Fluorescence Enhancement of Albumin-Chaperoned Cyanine Dyes from a Multiscale Computational Study. *J. Mater. Chem. C* **2023**, *11*, 7243−7251.
(39) Reindl, S.; Penzkofer, A.; Gong, S.-H.; Landthaler, M.; Szeimies, R.M.; Abels, C.; Baumler, W. Quantum Yield of Triplet Formation for Indocyanine Green. *J. Photoch. Photobio. A* **1997**, *105*, 65−68.
(40) Fan, H.; Fan, Y.; Du, W.; Cai, R.; Gao, X.; Liu, X.; Wang, H.; Wang, L.; Wu, X. Enhanced Type I Photoreaction of Indocyanine Green: Via Electrostatic-Force-Driven Aggregation. *Nanoscale* **2020**, *12*, 9517−9523.
(41) Levitus, M.; Ranjit, S. Cyanine Dyes in Biophysical Research: The Photophysics of Polymethine Fluorescent Dyes in Biomolecular Environments. *Q. Rev. Biophy.* **2011**, *44*, 123−151.
(42) Zhu, N.; Xu, J.; Su, Q.; Han, T.; Zhou, D.; Zhang, Y.; Zhu, S. Site-Specific Albumin Tagging with NIR-II Fluorogenic Dye for High-Performance and Super-Stable Bioimaging. *Theranostics* **2024**, *14*, 1860−1872.
(43) Onda, N.; Kimura, M.; Yoshida, T.; Shibutani, M. Preferential Tumor Cellular Uptake and Retention of Indocyanine Green for in Vivo Tumor Imaging. *Int. J. Cancer* **2016**, *139*, 673−682.
(44) Gong, B.; Shen, Y.; Li, H.; Li, X.; Huan, X.; Zhou, J.; Chen, Y.; Wu, J.; Li, W. Thermo-Responsive Polymer Encapsulated Gold Nanorods for Single Continuous Wave Laser-Induced Photodynamic/Photothermal Tumour Therapy. *J. Nanobiotechnol.* **2021**, *19*, 41.
(45) Zheng, X.; Zhou, F.; Wu, B.; Chen, W. R.; Xing, D. Enhanced Tumor Treatment Using Biofunctional Indocyanine Green-Containing Nanostructure by Intratumoral or Intravenous Injection. *Mol. Pharmaceutics* **2012**, *9*, 514−522.
(46) Buckle, T.; van Willigen, D. M.; Spa, S. J.; Hensbergen, A. W.; van der Wal, S.; de Korne, C. M.; Welling, M. M.; van der Poel, H. G.; Hardwick, J. C. H.; van Leeuwen, F. W. B. Tracers for Fluorescence-Guided Surgery: How Elongation of the Polymethine Chain in Cyanine Dyes Alters the Pharmacokinetics of a (Bimodal) c[RGDyK] Tracer. *J. Nucl. Med.* **2018**, *59*, 986−992.
(47) Schreiber, C. L.; Zhai, C.; Dempsey, J. M.; Mcgarraugh, H. H.; Matthews, B. P.; Christmann, C. R.; Smith, B. D. Paired Agent Fluorescence Imaging of Cancer in a Living Mouse Using Preassembled Squaraine Molecular Probes with Emission Wavelengths of 690 and 830 nm. *Bioconjugate Chem.* **2020**, *31*, 214−223.
(48) Gamage, R. S.; Li, D.-H.; Schreiber, C. L.; Smith, B. D. Comparison of cRGDfK Peptide Probes with Appended Shielded Heptamethine Cyanine Dye (s775z) for Near Infrared Fluorescence Imaging of Cancer. *ACS Omega* **2021**, *6*, 30130−30139.
(49) Shibasaki, Y.; Sakaguchi, T.; Hiraide, T.; Morita, Y.; Suzuki, A.; Baba, S.; Setou, M.; Konno, H. Expression of Indocyanine Green-Related Transporters in Hepatocellular Carcinoma. *J. Surg. Res.* **2015**, *193*, 567−576.
(50) Shibasaki, Y.; Morita, Y.; Sakaguchi, T.; Konno, H. Indocyanine Green-Related Transporters in Hepatocellular Carcinoma. In *ICG Fluorescence Imaging and Navigation Surgery*; Kusano, M., Kokudo, N., Tori, M., Kaibori, M., Eds.; Springer, 2016; pp 351−362; DOI: 10.1007/978-4-431-55528-5_32.
(51) Berezin, M. Y.; Guo, K.; Akers, W.; Livingston, J.; Solomon, M.; Lee, H.; Liang, K.; Agee, A.; Achilefu, S. Rational Approach to Select Small Peptide Molecular Probes Labeled with Fluorescent Cyanine Dyes for in Vivo Optical Imaging. *Biochemistry* **2011**, *50*, 2691−2700.
(52) Li, C.; Zhou, S.; Chen, J.; Jiang, X. Fluorescence Imaging of Inflammation with Optical Probes. *Chem. Biomed. Imaging* **2023**, *1*, 495−508.
(53) Gedat, E.; Berger, J.; Kiesel, D.; Failli, V.; Briel, A.; Welker, P. Features Found in Indocyanine Green-Based Fluorescence Optical Imaging of Inflammatory Diseases of the Hands. *Diagnostics* **2022**, *12*, 1775.
(54) Beringhs, A. O.; Singh, S. P.; Valdez, T. A.; Lu, X. Sublingual Indocyanine Green Films for Non-Invasive Swallowing Assessment and Inflammation Detection through NIR/SWIR Optical Imaging. *Sci. Rep-UK* **2020**, *10*, No. 14003.
(55) Xiao-Ping, W.; Rong, L.; Min, Z.; Lulu, Z.; Hongyan, R.; Meiling, P.; Gao-Hui, Z. Coumarin-Based Fluorescence Turn-on Probes for High Selectivity Peroxynitrite Detection and Imaging in Living Cells and γ-Carrageenan-Induced Inflammatory Tissue and Mice. *Microchem. J.* **2022**, *183*, No. 108003.
(56) Bao, K.; Tully, M.; Cardenas, K.; Wang, H.; Srinivas, S.; Rho, J.; Jeon, O. H.; Dinh, J.; Yokomizo, S.; McDonnell, R.; et al. Ultralow Background Near-Infrared Fluorophores with Dual-Channel Intra-

operative Imaging Capability. *Adv. Healthc. Mater.* **2023**, *12*, No. e2203134.
(57) Li, D.; Schreiber, C. L.; Smith, B. D. Sterically Shielded Heptamethine Cyanine Dyes for Bioconjugation and High Performance Near-Infrared Fluorescence Imaging. *Angew. Chem., Int. Ed.* **2020**, *59*, 12154−12161.
(58) Miller, J.; Wang, S. T.; Orukari, I.; Prior, J.; Sudlow, G.; Su, X.; Liang, K.; Tang, R.; Hillman, E. M. C.; Weilbaecher, K. N.; et al. Perfusion-Based Fluorescence Imaging Method Delineates Diverse Organs and Identifies Multifocal Tumors Using Generic near-Infrared Molecular Probes. *J. Biophotonics* **2018**, *11*, No. e201700232.
(59) Jennings, D.; Raghunand, N.; Gillies, R. J. Imaging Hemodynamics. *Cancer Metast. Rev.* **2008**, *27*, 589−613.
(60) Yang, C.; Wang, H.; Yokomizo, S.; Hickey, M.; Chang, H.; Kang, H.; Fukuda, T.; Song, M. Y.; Lee, S. Y.; Park, J. W.; Bao, K.; Choi, H. S. ZW800-PEG: A Renal Clearable Zwitterionic Near-Infrared Fluorophore for Potential Clinical Translation. *Angew. Chem., Int. Ed.* **2021**, *60*, 13847−13852.
(61) Hillman, E. M. C.; Moore, A. All-Optical Anatomical Co-Registration for Molecular Imaging of Small Animals Using Dynamic Contrast. *Nat. Photonics* **2007**, *1*, 526−530.
(62) Jagtap, J.; Sharma, G.; Parchur, A. K.; Gogineni, V.; Bergom, C.; White, S.; Flister, M. J.; Joshi, A. Methods for Detecting Host Genetic Modifiers of Tumor Vascular Function Using Dynamic Near-Infrared Fluorescence Imaging. *Biomed. Opt. Express* **2018**, *9*, 543.
(63) Sindrewicz, P.; Li, X.; Yates, E. A.; Turnbull, J. E.; Lian, L. Y.; Yu, L. G. Intrinsic Tryptophan Fluorescence Spectroscopy Reliably Determines Galectin-Ligand Interactions. *Sci. Rep.* **2019**, *9*, No. 11851.
(64) Ghasemi, M.; Turnbull, T.; Sebastian, S.; Kempson, I. The MTT Assay: Utility, Limitations, Pitfalls, and Interpretation in Bulk and Single-Cell Analysis. *Int. J. Mol. Sci.* **2021**, *22*, 12827.

https://doi.org/10.1021/cbmi.4c00008
Chem. Biomed. Imaging 2024, 2, 384−397